NANO LETTERS

pubs.acs.org/NanoLett

Letter

Simultaneously Enhancing Brightness and Purity of WSe_2 Single Photon Emitter Using High-Aspect-Ratio Nanopillar Array on Metal

Mayank Chhaperwal, Himanshu Madhukar Tongale, Patrick Hays, Kenji Watanabe, Takashi Taniguchi, Seth Ariel Tongay, and Kausik Majumdar*

Cite This: *Nano Lett.* 2024, 24, 12461−12468

Read Online

ACCESS | Metrics & More | Article Recommendations | Supporting Information

ABSTRACT: A monolayer semiconductor transferred on nanopillar arrays provides site-controlled, on-chip single photon emission, which is a scalable light source platform for quantum technologies. However, the brightness of these emitters reported to date often falls short of the perceived requirement for such applications. Also, the single photon purity usually degrades as the brightness increases. Hence, there is a need for a design methodology to achieve an enhanced emission rate while maintaining high single photon purity. By using WSe_2 on high-aspect-ratio (~3, at least 2-fold higher than previous reports) nanopillar arrays, here we demonstrate >10 MHz single photon emission rate in the 770−800 nm band that is compatible with quantum memory and repeater networks (Rb-87-D1/D2 lines) and satellite quantum communication. The emitters exhibit excellent purity (even at high emission rates) and improved out-coupling due to the use of a gold back reflector that quenches the emission away from the nanopillar.

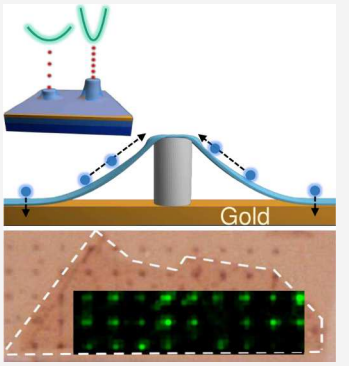

KEYWORDS: *Single photon source, quantum emitter, WSe_2, 2D materials, brightness, second-order correlation*

On-chip single photon emitters (SPEs) provide a scalable approach toward photonics-based quantum technologies such as quantum computing, quantum communication, and quantum metrology.[1,2] SPEs based on transition metal dichalcogenides (TMDCs) are highly attractive as the two-dimensional nature of the host provides several possible advantages, such as, ease of integration with photonic/plasmonic cavities and waveguides,[3−8] low outcoupling loss,[3,5−7] gate induced spectral tunability,[9−12] and the possibility of integration with electrical excitation scheme.[11,13,14] In nanopillar-based SPE implementations, the strain introduced on the monolayer through a nanopillar helps funnel excitons[15−19] toward the defect located at the pillar site, improving the net quantum efficiency of single photon emission.[20,21] While such sources are highly promising due to the spatially deterministic nature of the array of quantum emitters at the lithographically defined positions,[4,8,9,20−23] there are two key challenges that must be addressed for practical quantum applications.

These two challenges are illustrated in Figure 1, where we plot the measured brightness (in counts per second) as a function of single photon purity [in terms of $g^{(2)}(0)$] for reported TMDC-based SPEs.[3−5,8,24−26] The first observation is that the overall brightness is, in general, low, both with respect to other competing technologies (for example, quantum dots exhibiting several tens of MHz[27−29]) as well as the perceived requirement for several quantum technologies (in GHz, see[29,30]). The emission intensity from TMDC-based SPEs usually saturates much earlier than the rate suggested by their

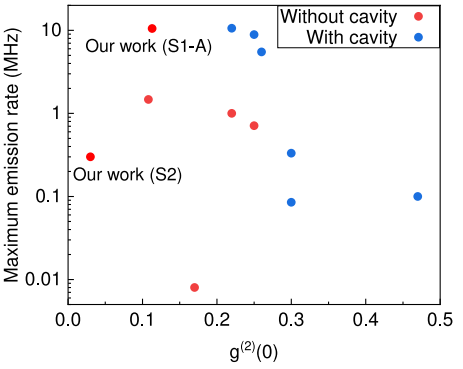

Figure 1. Status of TMDC-based single photon emitters and benchmarking. Brightness (in terms of maximum collected emission rate in MHz) against single photon purity [in terms of $g^{(2)}(0)$] plotted for reported TMDC-based single photon emitters.[3−5,8,24−26] We have selected only those reports having scalable architecture and spatially deterministic SPE. Works implementing a photonic/plasmonic cavity are encoded in blue symbols, and those without cavities are encoded in red symbols. The plot also shows the results from this work having two different aspect ratios of pillars (samples S1-A and S2).

Received: July 4, 2024
Revised: September 20, 2024
Accepted: September 20, 2024
Published: September 25, 2024

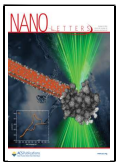

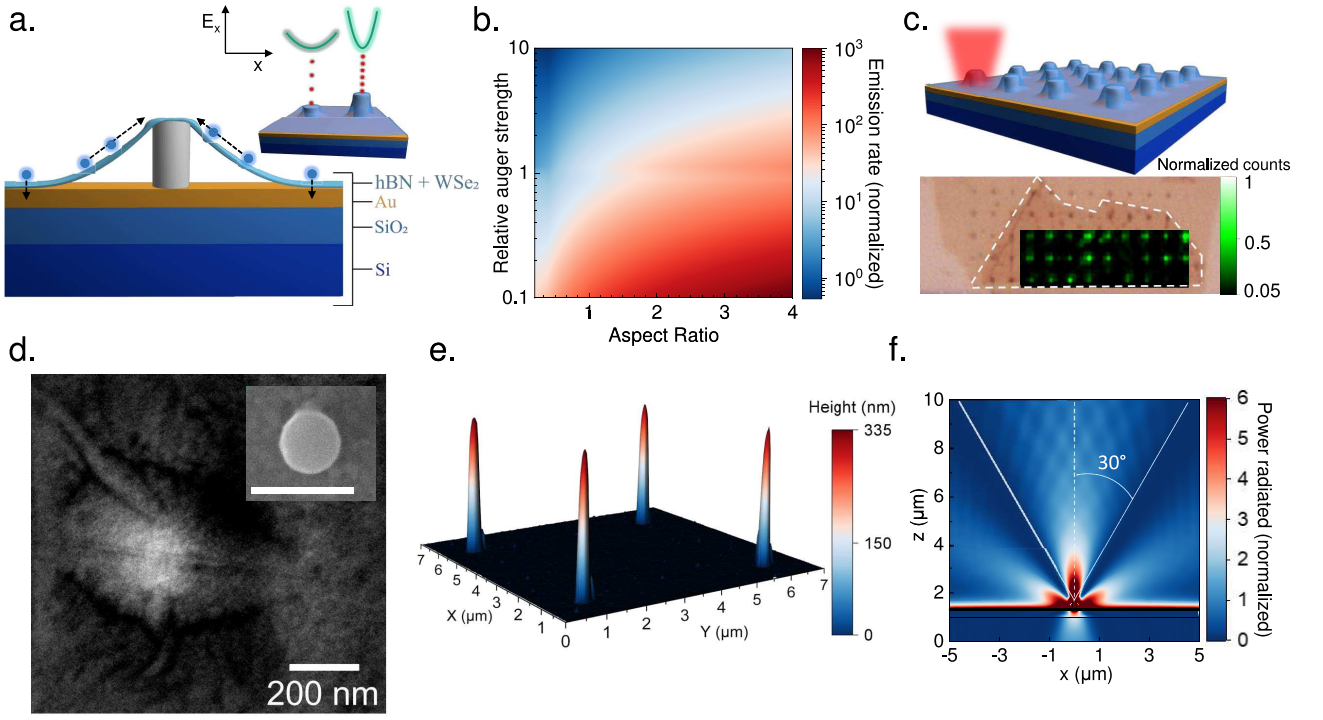

Figure 2. Design of the single photon emitter. (a) Schematic cross section showing the different layers in the SPE. Inset: Schematic showing a comparison of shorter versus taller pillars with respect to their single photon emission rates. Excitonic bands showing different band-bending gradients are also shown. (b) Color plot from our model showing the variation of normalized maximum emission rate achievable as a function of the nanopillar aspect ratio and Auger coefficient. (c) Top panel: Schematic showing the array of nanopillars covered with TMD monolayer and hBN. Individual nanopillars are spaced by 5 μm such that the excitation laser spot covers only one of the nanopillars. Bottom panel: Optical image of the fabricated device with WSe_2 monolayer (bounded by white dashed line) covering the array of nanopillars. Overlaid is the result from the PL map showing bright emission spots coinciding with the nanopillar locations. (d) SEM image of the WSe_2 monolayer on a nanopillar. The nanopillar touches the gold-coated substrate around 250−300 nm away from the center of the nanopillar. The scale bar is 200 nm. Inset: SEM image of a bare nanopillar showing a diameter of around 110 nm (scale bar is 200 nm). (e) AFM image of a section of the fabricated nanopillar array showing a set of 4 nanopillars with height around 330 nm. (f) Result from the FDTD simulation showing the spatial distribution of the emission pattern of the SPE on the pillar. The solid white lines indicate the collection angle of our objective with an NA of 0.5.

lifetime. Auger annihilation has been suggested as the limiting factor for such early saturation.[8] While methods, such as photonic/plasmonic cavities,[3,8] have improved the brightness of the SPEs, there is still a pressing need for further improvement.

While good single photon purity has been demonstrated in the past,[20−22] the second observation from Figure 1 is the lack of reports with simultaneous observation of low $g^{(2)}(0)$ and high emission rate. The diffraction-limited laser spot is much larger than the nanopillar diameter for optical excitation. This causes considerable contribution from the surrounding regions to the collected photon count. Unlike the SPE, the background emission is not bottlenecked by a single level and, hence, does not have a strong saturating behavior with increasing power. Accordingly, it often starts to dominate the SPE emission at higher excitation power, degrading the single photon purity.

The aim of this work is to bridge the above-mentioned gaps by introducing high-aspect-ratio nanopillars on metal film to significantly improve the brightness of the TMDC-based SPEs while maintaining an excellent single photon purity at high emission rates - a step toward practical SPE solution for various quantum technologies.

Transferring a monolayer on a nanopillar introduces a nonuniform strain in the flake, with maximum strain at the pillar site. The band gap of the monolayer reduces with such local strain,[15−17] causing excitons to funnel toward the pillar site. A point defect on the pillar captures these available excitons and emits subsequently, giving rise to single photon emission.

The overall design of our SPE array employing monolayer WSe_2 on nanopillars has three important features, as illustrated schematically in Figure 2a. The design is inspired by our model (discussed later) predicted brightness of the SPE as a function of Auger strength and pillar aspect ratio (height:diameter, denoted as α), shown in Figure 2b. The results suggest that Auger-induced exciton annihilation in the strain-induced potential well on the nanopillar prevents the SPE from achieving its lifetime-limited emission rate. However, a higher α helps to overcome this limitation through stronger exciton funneling toward the pillar site (see inset of Figure 2a). One drawback of high-aspect-ratio nanopillars made of hard material, such as SiO_2, having a rough top surface, is the possibility of piercing through the flake during the transfer process.[21,31] To mitigate this, we fabricate the nanopillars using a negative photoresist followed by baking (see Methods in Supporting Information 1). The polymer-based negative resist provides a comparatively softer structure and a smoother top surface. We fabricate an array of such nanopillars, keeping a pillar-to-pillar spacing (5 μm) well beyond the excitation laser spot size (~1.5 μm) so that only one pillar is excited at a time (top panel of Figure 2c for a schematic view and the bottom panel for an optical image). Figure 2d shows an SEM image of

https://doi.org/10.1021/acs.nanolett.4c03168
Nano Lett. 2024, 24, 12461−12468

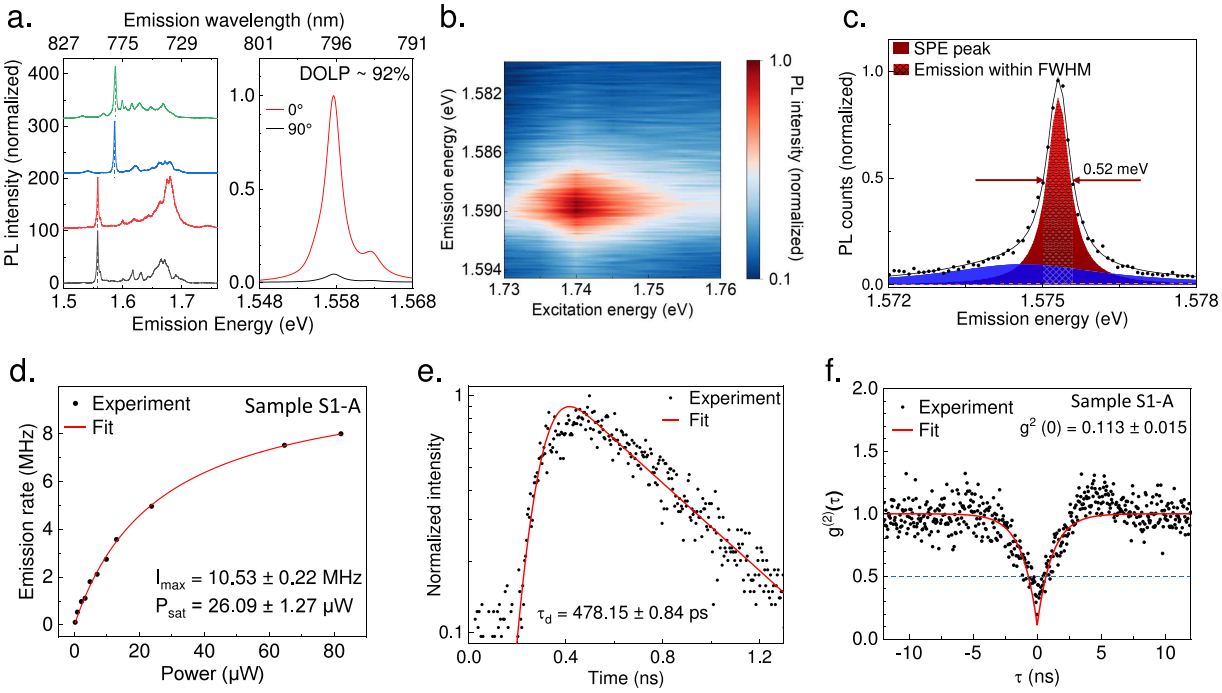

Figure 3. Characterization of the single photon emitter. (a) Left panel: PL spectra from four different nanopillar sites. The spectral location of the SPEs is marked by dashed vertical lines. Right panel: Polarization resolved PL spectrum of the SPE peak showing a DOLP of ∼92%. (b) Photoluminescence excitation measurement showing an enhancement in the SPE emission rate when the excitation is resonant to the free exciton energy of WSe_2. (c) Fitting of an SPE peak (data in black symbols and total fit in black solid trace) with Voigt functions and a background (orange dashed trace). The fitted peak (in red) is then integrated within its fwhm limits (black hatched portion) to calculate the integrated emission counts, thus removing the contribution from nearby peaks and background emission. The data shows a total measured line width of 520 μeV. (d) Integrated emission count rate from (c) plotted as a function of excitation power. The data fits with a saturation equation, giving a maximum emission rate of 10.53 ± 0.22 MHz and a saturation power of 26.09 μW. (e) TRPL results (data in black symbols and fitting in red trace) to characterize the formation time and the lifetime of the defect state. t = 0 ns marks the location of the laser pulse firing. (f) Second-order correlation measurement to quantify the purity of the SPE (experimental data in symbols and fitting in the red trace).

a single nanopillar with WSe_2 monolayer on top. The inset is an SEM image of a bare nanopillar with a diameter of about 110 nm. AFM measurement indicates a height of about 330 nm (Figure 2e). This gives us $\alpha \sim 3$, significantly higher than previous reports.[20−22]

Second, encapsulating TMDCs with hBN smoothens the inhomogeneous potential fluctuation and screens the inter-exciton interaction. This reduces the Auger coefficient significantly through suppressed interaction among locally trapped excitons.[32−34] Accordingly, we transfer a few-layer hBN flake on top of the monolayer/nanopillar stack. However, no hBN layer is introduced between the monolayer and the nanopillar to avoid a possible reduction in the strain.

Finally, in order to improve single photon purity, we mitigate the issue of the laser excitation spot being much larger than the nanopillar area by fabricating the nanopillars on gold-coated substrate. The part of the monolayer away from the nanopillar touches the gold film (Figure 2a), and the emission from those regions is almost completely quenched due to nonradiative charge transfer to gold.[35] This allows us to collect the emission only from the nanopillar region selectively. To support this claim, we perform a photoluminescence (PL) scan on the sample at 295 K around the free exciton emission energy (excited using 532 nm laser), and the integrated emission intensity is overlaid on the optical image (bottom panel of Figure 2c). The bright emission spots coincide with the location of the nanopillars in the optical image. A line cut from the PL map is presented in Supporting Information 2. The emission from the flake away from the nanopillar is almost completely quenched. On the other hand, excitons funnel to the nanopillar locations from the suspended regions, providing high brightness at the pillar site (schematic in Figure 2a). Most of the pillars covered by the monolayer show bright emission, suggesting high yield and minimal damage to the flake during the transfer process. Finally, the gold-coating acts as a back-reflector, improving the out-coupling of the emitted photons as depicted from the simulated emission pattern (Figure 2f) using 2D finite-difference time-domain (FDTD) method.

We refer to this SPE stack (with $\alpha = 3$) as structure S1 and prepare three different samples (S1-A, S1-B, and S1-C) containing arrays of nanopillars.

Figure 3a (left panel) shows representative PL emission spectra from four different nanopillars. The vertical dashed lines indicate the spectral position of the defect emission functioning as an SPE around 1.55−1.61 eV. The corresponding emission wavelength is in the 770−800 nm band and is thus suitable for quantum memory and repeater networks (being close to the Rb-87-D1/D2 line)[36] and satellite communication applications.[37] Note that the SPE peak is red-shifted compared to the broad defect and multiparticle emission of WSe_2 and, thus, is relatively free from background emission. Figure 3a (right panel) shows a high (∼92%) degree of linear polarization (DOLP) of these peaks. The DOLP value remains independent of the direction of the polarization of the excitation, suggesting the intrinsic linearly polarized nature of the SPE.

https://doi.org/10.1021/acs.nanolett.4c03168
Nano Lett. 2024, 24, 12461−12468

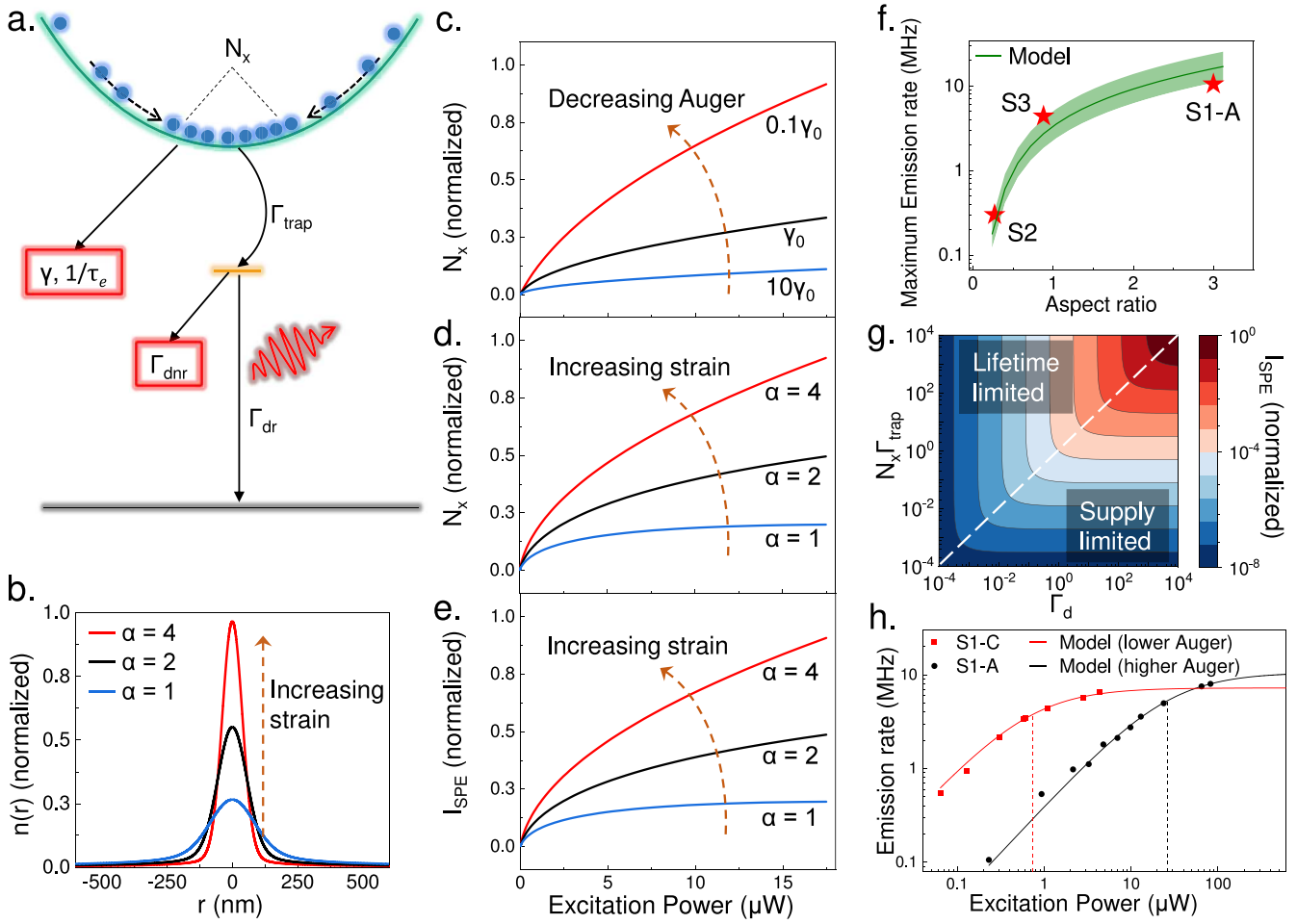

Figure 4. Single photon emitter model. (a) Schematic diagram showing the mechanism of exciton funneling in the strain-induced potential well and capture by the defect state. The processes involved at different stages are also illustrated. (b) Exciton density as a function of radial distance from the center of the pillar with varying pillar aspect ratio (α). (c, d) Exciton population near the center of the nanopillar (N_x) as a function of excitation power with (c) varying Auger coefficient relative to a base value γ_0 for a fixed aspect ratio of the pillar and (d) varying aspect ratio of the pillar for a fixed Auger coefficient. (e) SPE emission intensity as a function of excitation power with a varying aspect ratio (α) of the pillar. (f) Fitting of the model (in the green trace) with the experimentally measured maximum emission rate from samples S1-A, S2, and S3 (in red star symbols) as a function of pillar aspect ratio. The shaded portion demonstrates a ± 10% variation in the model parameters. (g) Maximum SPE emission intensity (normalized) achievable by varying the supply to the defect state ($N_x\Gamma_{trap}$) and total decay rate (Γ_d) of the defect state, for a given quantum efficiency. The dashed line indicates $\Gamma_d = N_x\Gamma_{trap}$ segregating the *supply-limited* regime from the *lifetime-limited* one. (h) Power dependent emission rate for S1-A (in black symbols) and S1-C (in red symbols) along with model fitting (solid traces). The fitted Auger coefficient for the red trace is about 100-fold smaller than the black trace. The dashed vertical lines indicate the corresponding saturation powers (0.74 μW for S1-C and 26.09 μW for S1-A).

The SPE peak intensity strongly depends on the excitation wavelength. As an example, we choose an emitter around 1.59 eV and find that the peak intensity is highest when the excitation is resonant to the WSe_2 free exciton (Figure 3b).

The sharpest peak we measured has a full-width-at-half-maximum (fwhm) of 520 μeV and is shown in Figure 3c. We perform incident power (P) dependent PL measurement to characterize the brightness of the SPE. Figure 3c shows the method used to calculate the emission rate of the SPE. The peaks are fitted using a Voigt function, and the contributions from the side peaks and the background are removed. The SPE peak is then integrated within its fwhm (marked by the shaded portion) and then adjusted for our system efficiency of 5.1%. This integrated emission intensity (I) of the SPE peak is plotted against P in Figure 3d, and the data is fitted with $I = I_{sat} \cdot \{P/(P + P_{sat})\}$. This gives us a maximum emission rate of 10.53 ± 0.22 MHz, which is free from other spurious contributions. Note that we deliberately do not report the collected SPAD count rate. This is because even after spectral filtering, the photons collected by the SPAD have a component arising from the background and side peaks. This component increases rapidly with the incident power and thus results in erroneous inflation of the measured emission rate of the device (Supporting Information 3). Power dependent emission rate from three other fabrication runs is shown in Supporting Information 4, suggesting a repeatable high emission rate from our samples.

Note that this is the emission rate collected by the objective [numerical aperture (NA) of 0.5] and is not corrected for the collection angle limited by its NA. Our FDTD simulation (Figure 2f) predicts that 33.93% of the total photons emitted by the dipole above the substrate surface are collected by our objective. This gives an emission rate of ~31 MHz above the surface of the substrate. Collection efficiency with respect to

https://doi.org/10.1021/acs.nanolett.4c03168
Nano Lett. 2024, 24, 12461−12468

the total emission is 28.36%, giving a total emission rate of ∼37 MHz. The FDTD simulation also rules out the existence of Purcell enhancement in the structure.

We perform time-resolved photoluminescence (TRPL) measurement to characterize the lifetime[5,6,14,20,21,25,38−42] of the trapped exciton in the quantum emitter (Figure 3e). After fitting with a decaying exponential convoluted with a Gaussian rise function (see Methods in Supporting Information 1), we extract a lifetime (τ_d) of 487.15 ± 0.84 ps and a formation time (τ_f) of 541 ± 0.95 ps.

To characterize the single photon nature of the emission, we perform second-order correlation measurement in a Hanbury Brown and Twiss (HBT) setup. After deconvolution from the Gaussian instrument response function (IRF) (see Methods in Supporting Information 1), we extract a $g^{(2)}(0)$ value of 0.113 ± 0.015 at a high collected count rate of 1 MHz. Note that the fit does not involve any background correction. The maintained single photon purity at this high emission rate confirms the functioning of the gold-coated substrate as an excellent background suppressor. Spectral separation of the SPE from typical broad defect emission of WSe_2 also helps because the tail of such broad emission does not intrude into the spectral region of the SPE. The corresponding $g^{(2)}(\tau)$ plot for the sample exhibiting the narrowest SPE peak (spectrum in Figure 3c) is shown in Supporting Information 5. Also, in Supporting Information 6, we show $g^{(2)}(\tau)$ from a lower-aspect-ratio pillar (sample S2) with a $g^{(2)}(0)$ of 0.024 ± 0.017.

In Figure 1, we compare our results with reported data[3−5,8,24−26] in the space of maximum emission rate versus $g^{(2)}(0)$, suggesting a superior emission rate while maintaining improved single photon purity. The emission rate from our high aspect-ratio pillars is 7-fold higher than the previous highest reported rate from pillars without cavities and is on par with works using photonic/plasmonic cavities.

We model the SPE as two interconnected subsystems (see Figure 4a): (a) exciton funneling in the strain-induced potential well, and (b) these funneled excitons acting as a reservoir for exciting the defect-based atom-like two-level system, which then relaxes to the ground state, emitting single photons. We discuss these two parts of the model below.

The rate equation for the exciton density $n(r, t)$ at a radial distance r from the center of the strain well is given by (see Supporting Information 7 for derivation):

$$\frac{\partial n(r,t)}{\partial t} = -\frac{\partial F(r)}{\partial r} + g(r) - \frac{n(r)}{\tau_e} - \gamma n^2(r) \tag{1}$$

Here the first term on the right-hand side captures both the out-diffusion of excitons due to concentration gradient and the drift of excitons toward the pillar center due to strain gradient, F being the total outward flux of the excitons. $g(r)$ is the generation rate with a spatial Gaussian profile, τ_e is the effective lifetime of the exciton (combining both radiative and nonradiative pathways, other than Auger process) and γ is the Auger coefficient.

The calculated steady-state $\left(\frac{\partial n(r,t)}{\partial t} = 0\right)$ exciton density profile $[n(r)]$ is plotted in Figure 4b, suggesting stronger exciton funneling as α increases. In Figure 4c, we plot the total exciton population $[N_x = \int_0^{r_0} 2\pi r n(r) dr]$ near the center of the nanopillar as a function of P for different γ (r_0 is taken as 1 nm in the plots). The results indicate a saturation in N_x with P, and N_x saturates at a lower value for higher γ. This suggests that Auger annihilation, being a quadratic function, is the primary bottleneck to increase N_x. A higher α that induces stronger exciton funneling could be a way to mitigate such Auger-mediated saturation, as illustrated in Figure 4d.

An exciton from the reservoir that is in the vicinity is captured by a point defect, populating an atom-like two-level system consisting of the defect state and the ground state (Figure 4a). The SPE emission energy is ∼200 meV lower than the free exciton (Figure 3a). The hybridization of this defect state with the dark exciton band[43−47] is thus unlikely in our samples because of the large energy separation between them.

The steady-state emission rate of the SPE is given by (see Supporting Information 9 for derivation):

$$I_{SPE} = \Gamma_{dr}\left(\frac{N_x\Gamma_{trap}}{N_x\Gamma_{trap} + \Gamma_d}\right) \tag{2}$$

Here Γ_{trap} quantifies the rate of capture of an individual exciton by the defect. $\Gamma_d = \frac{1}{\tau_d} = \Gamma_{dr} + \Gamma_{dnr}$ is the effective rate of relaxation from the defect state, considering both radiative (Γ_{dr}) and nonradiative (Γ_{dnr}) pathways. In Figure 4e, the calculated I_{SPE} is plotted against incident power for varying α, indicating an effective enhancement of the maximum emission rate with pillar aspect ratio. The variation of the calculated maximum emission rate is shown earlier (Figure 2b) in a color plot as a function of the Auger coefficient and pillar aspect ratio.

To verify that such a high emission rate results from the increased strain due to the higher aspect ratio of our nanopillars, we prepare two other samples (S2 and S3) with a lower aspect ratio of α = 0.27 and α = 0.88 respectively. The maximum collected rate measured from these devices is plotted in Figure 4f. The model provides an excellent fit to the experimentally observed maximum emission rate as a function of α, verifying the validity of the model.

Note that $N_x\Gam_{trap}$ provides a good estimate of the rate of formation of the defect-bound exciton (see Supporting Information 8 and 9, and hence $N_x\Gamma_{trap} \approx \frac{1}{\tau_f}$. With this approximation, eq 2 reduces to the expected form:

$$I_{SPE} = \eta \times \frac{1}{\tau_f + \tau_d} \tag{3}$$

Here $\eta = \frac{\Gamma_{dr}}{\Gamma_d}$ is the quantum efficiency of the defect emission.

Equations 2 and 3 provide key insights into the possible ways to enhance the SPE emission rate, and the results are shown in Figure 4g. For example, when $N_x\Gamma_{trap} \ll \Gamma_d$, that is, when the defect state is starved of exciton supply from the reservoir (lower half in Figure 4g, denoted as "*supplylimited*"), $I_{SPE} \approx \eta N_x\Gamma_{trap} \approx \eta/\tau_f$ and hence I_{SPE} exactly follows N_x. Since N_x saturates at higher excitation power, I_{SPE} also saturates prematurely without reaching the true lifetime limited rate of Γ_{dr}. Such saturation behavior thus does not arise from the limit of a 2-level quantum system. We believe a majority of the reported TMDC-based SPEs to date fall under this regime. Mitigating the Auger-induced early saturation by increasing the nanopillar aspect ratio can improve the emission rate in this regime (see Figure 4e).

On the other hand, when $N_x\Gamma_{trap} \gg \Gamma_d$, that is, when the defect state is not starved by the supply of excitons (upper half in Figure 4g, denoted as "*lifetime-limited*"), $I_{SPE} \approx \Gamma_{dr}$ indicating radiative lifetime-limited emission rate, and thus further

https://doi.org/10.1021/acs.nanolett.4c03168
Nano Lett. 2024, 24, 12461−12468

increasing the supply through enhanced pillar aspect ratio or reducing Auger recombination is not effective anymore in this regime. This also means that with adequate supply, I_{SPE} can achieve Γ_{dr} irrespective of the value of Γ_{dnr}.

To verify the model, in Supporting Information 10, we compare the emission spectra of samples S1-A and S1-C. S1-C uses the same aspect ratio pillars (α = 3) as S1-A, however, a different batch of WSe_2 that exhibits relatively weak background emission. This suggests a smoother potential profile and, thus, likely suppressed Auger loss due to reduced exciton localization.[32−34] The defect peak emission is slightly blue-shifted to 1.6 eV in this sample. Interestingly, we achieve a similar maximum count rate of 7.4 ± 0.17 MHz; however, the saturation excitation power (P_{sat}) is ∼35-fold lower compared with S1-A. By varying the Auger coefficient for S1-A and S1-C, our model provides an excellent fit (Figure 4h) with the experimentally obtained emission rate as a function of excitation power for both the samples.

The second factor on the right side in eq 2, that is, $\beta \equiv \frac{N_x\Gamma_{trap}}{N_x\Gamma_{trap}+\Gamma_d}$ provides a quantitative estimate of the degree of supply limitation, with β close to zero indicating strong supply limitation, and β close to unity indicating lifetime-limited regime. In our sample S1-A with a high pillar aspect ratio, the extracted values of τ_f and τ_d from TRPL suggest $\beta \approx 0.47$. This justifies the lack of a proportionate increment in the maximum emission rate in S1-C (with respect to S1-A) in spite of significant suppression of the Auger coefficient.

Finally, with the estimated total emission rate of ∼37 MHz and $\beta \approx 0.47$, eq 2 suggests a radiative rate (Γ_{dr}) of ∼79 MHz and hence a radiative lifetime of ∼12.6 ns. Thus, there is a scope for further optimization of the pillar aspect ratio to improve the maximum emission rate by nearly a factor of 2. However, a significant enhancement in the emission rate beyond this would require improving Γ_{dr}, possibly through cavity and material design, which could lead to scalable and highly pure single photon emission with rates beyond 100 MHz. Further, in the current work, there is a lack of precise control on the SPE emission wavelength, which could be addressed in the future through an external electric field-induced Stark shift.

■ ASSOCIATED CONTENT

Data Availability Statement

Data available on reasonable request from the corresponding author.

Supporting Information

The Supporting Information is available free of charge at https://pubs.acs.org/doi/10.1021/acs.nanolett.4c03168.

Fabrication and characterization methods, line cut from PL mapping of emitters, SPAD count rate versus pure SPE count rate, emission rate data from additional samples, single photon purity data from additional samples, description of the model, description of two-level emitter, SPE model details, and comparison of devices with higher and lower Auger coefficients (PDF)

■ AUTHOR INFORMATION

Corresponding Author

Kausik Majumdar − *Department of Electrical Communication Engineering, Indian Institute of Science, Bangalore 560012, India;* orcid.org/0000-0002-6544-7829; Email: kausikm@iisc.ac.in

Authors

Mayank Chhaperwal − *Department of Electrical Communication Engineering, Indian Institute of Science, Bangalore 560012, India;* orcid.org/0009-0001-7142-5140

Himanshu Madhukar Tongale − *Department of Electrical Communication Engineering, Indian Institute of Science, Bangalore 560012, India;* orcid.org/0009-0009-4731-6313

Patrick Hays − *Materials Science and Engineering, School for Engineering of Matter, Transport and Energy, Arizona State University, Tempe, Arizona 85287, United States*

Kenji Watanabe − *Research Center for Electronic and Optical Materials, National Institute for Materials Science, Tsukuba 305-044, Japan;* orcid.org/0000-0003-3701-8119

Takashi Taniguchi − *Research Center for Materials Nanoarchitectonics, National Institute for Materials Science, Tsukuba 305-044, Japan;* orcid.org/0000-0002-1467-3105

Seth Ariel Tongay − *Materials Science and Engineering, School for Engineering of Matter, Transport and Energy, Arizona State University, Tempe, Arizona 85287, United States;* orcid.org/0000-0001-8294-984X

Complete contact information is available at: https://pubs.acs.org/10.1021/acs.nanolett.4c03168

Notes

The authors declare no competing financial interest.

■ ACKNOWLEDGMENTS

K.M. acknowledges useful discussion with Naresh Babu Pendyala from ISRO. This work was supported in part by a Core Research Grant from the Science and Engineering Research Board (SERB) under Department of Science and Technology (DST), grants from Indian Space Research Organization (ISRO), a grant under SERB TETRA, a grant from I-HUB QTF, IISER Pune, and a seed funding under Quantum Research Park (QuRP) from Karnataka Innovation and Technology Society (KITS), K-Tech, Government of Karnataka. K.W. and T.T. acknowledge support from the JSPS KAKENHI (Grant Numbers 21H05233 and 23H02052) and World Premier International Research Center Initiative (WPI), MEXT, Japan. S.A.T. acknowledges direct support from DOE-SC0020653 (materials synthesis), NSF ECCS 2052527, DMR 2111812, and CMMI 2129412. The use of facilities within the Eyring Materials Center at Arizona State University is partly supported by NNCI-ECCS-1542160.

■ REFERENCES

(1) Montblanch, A. R.-P.; Barbone, M.; Aharonovich, I.; Atature, M.; Ferrari, A. C. Layered materials as a platform for quantum technologies. *Nat. Nanotechnol.* **2023**, *18* (6), 555.

(2) Turunen, M.; Brotons-Gisbert, M.; Dai, Y.; Wang, Y.; Scerri, E.; Bonato, C.; Jons, K. D.; Sun, Z.; Gerardot, B. D. Quantum photonics with layered 2D materials. *Nature Reviews Physics* **2022**, *4* (4), 219.

(3) Luo, Y.; Shepard, G. D.; Ardelean, J. V.; Rhodes, D. A.; Kim, B.; Barmak, K.; Hone, J. C.; Strauf, S. Deterministic coupling of site-controlled quantum emitters in monolayer WSe_2 to plasmonic nanocavities. *Nat. Nanotechnol.* **2018**, *13* (12), 1137.

(4) Cai, T.; Kim, J.-H.; Yang, Z.; Dutta, S.; Aghaeimeibodi, S.; Waks, E. Radiative Enhancement of Single Quantum Emitters in WSe_2

Monolayers Using Site-Controlled Metallic Nanopillars. *ACS Photonics* **2018**, *5* (9), 3466.
(5) Peyskens, F.; Chakraborty, C.; Muneeb, M.; Van Thourhout, D.; Englund, D. Integration of single photon emitters in 2D layered materials with a silicon nitride photonic chip. *Nat. Commun.* **2019**, *10* (1), 4435.
(6) Iff, O.; Buchinger, Q.; Moczała-Dusanowska, M.; Kamp, M.; Betzold, S.; Davanco, M.; Srinivasan, K.; Tongay, S.; Anton-Solanas, C.; Hofling, S.; Schneider, C. Purcell-Enhanced Single Photon Source Based on a Deterministically Placed WSe_2 Monolayer Quantum Dot in a Circular Bragg Grating Cavity. *Nano Lett.* **2021**, *21* (11), 4715.
(7) Drawer, J.-C.; Mitryakhin, V. N.; Shan, H.; Stephan, S.; Gittinger, M.; Lackner, L.; Han, B.; Leibeling, G.; Eilenberger, F.; Banerjee, R.; Tongay, S.; Watanabe, K.; Taniguchi, T.; Lienau, C.; Silies, M.; Anton-Solanas, C.; Esmann, M.; Schneider, C. Monolayer-Based Single-Photon Source in a Liquid-Helium-Free Open Cavity Featuring 65% Brightness and Quantum Coherence. *Nano Lett.* **2023**, *23* (18), 8683.
(8) Sortino, L.; Zotev, P. G.; Phillips, C. L.; Brash, A. J.; Cambiasso, J.; Marensi, E.; Fox, A. M.; Maier, S. A.; Sapienza, R.; Tartakovskii, A. I. Bright single photon emitters with enhanced quantum efficiency in a two-dimensional semiconductor coupled with dielectric nano-antennas. *Nat. Commun.* **2021**, *12* (1), 6063.
(9) Mukherjee, A.; Chakraborty, C.; Qiu, L.; Vamivakas, A. N. Electric field tuning of strain-induced quantum emitters in WSe_2. *AIP Advances* **2020**, *10* (7), 075310.
(10) Schwarz, S.; Kozikov, A.; Withers, F.; Maguire, J. K.; Foster, A. P.; Dufferwiel, S.; Hague, L.; Makhonin, M. N.; Wilson, L. R.; Geim, A. K.; Novoselov, K. S.; Tartakovskii, A. I. Electrically pumped single-defect light emitters in WSe_2. *2D Materials* **2016**, *3* (2), 025038.
(11) Guo, S.; Germanis, S.; Taniguchi, T.; Watanabe, K.; Withers, F.; Luxmoore, I. J. Electrically Driven Site-Controlled Single Photon Source. *ACS Photonics* **2023**, *10* (8), 2549.
(12) Stevens, C. E.; Chuang, H.-J.; Rosenberger, M. R.; McCreary, K. M.; Dass, C. K.; Jonker, B. T.; Hendrickson, J. R. Enhancing the Purity of Deterministically Placed Quantum Emitters in Monolayer WSe_2. *ACS Nano* **2022**, *16* (12), 20956.
(13) So, J.-P.; Kim, H.-R.; Baek, H.; Jeong, K.-Y.; Lee, H.-C.; Huh, W.; Kim, Y. S.; Watanabe, K.; Taniguchi, T.; Kim, J.; Lee, C.-H.; Park, H.-G. Electrically driven strain-induced deterministic single-photon emitters in a van der Waals heterostructure. *Science Advances* **2021**, *7* (43), eabj31.
(14) Palacios-Berraquero, C.; Barbone, M.; Kara, D. M.; Chen, X.; Goykhman, I.; Yoon, D.; Ott, A. K.; Beitner, J.; Watanabe, K.; Taniguchi, T.; Ferrari, A. C.; Atature, M. Atomically thin quantum light-emitting diodes. *Nat. Commun.* **2016**, *7* (1), 12978.
(15) Johari, P.; Shenoy, V. B. Tuning the Electronic Properties of Semiconducting Transition Metal Dichalcogenides by Applying Mechanical Strains. *ACS Nano* **2012**, *6* (6), 5449.
(16) Shen, T.; Penumatcha, A. V.; Appenzeller, J. Strain Engineering for Transition Metal Dichalcogenides Based Field Effect Transistors. *ACS Nano* **2016**, *10* (4), 4712.
(17) Brooks, M.; Burkard, G. Theory of strain-induced confinement in transition metal dichalcogenide monolayers. *Phys. Rev. B* **2018**, *97* (19), 195454.
(18) Harats, M. G.; Kirchhof, J. N.; Qiao, M.; Greben, K.; Bolotin, K. I. Dynamics and efficient conversion of excitons to trions in non-uniformly strained monolayer WS_2. *Nat. Photonics* **2020**, *14* (5), 324.
(19) Niehues, I.; Schmidt, R.; Druppel, M.; Marauhn, P.; Christiansen, D.; Selig, M.; Berghauser, G.; Wigger, D.; Schneider, R.; Braasch, L.; Koch, R.; Castellanos-Gomez, A.; Kuhn, T.; Knorr, A.; Malic, E.; Rohlfing, M.; Michaelis de Vasconcellos, S.; Bratschitsch, R. Strain Control of Exciton−Phonon Coupling in Atomically Thin Semiconductors. *Nano Lett.* **2018**, *18* (3), 1751.
(20) Branny, A.; Kumar, S.; Proux, R.; Gerardot, B. D Deterministic strain-induced arrays of quantum emitters in a two-dimensional semiconductor. *Nat. Commun.* **2017**, *8* (1), 15053.
(21) Palacios-Berraquero, C.; Kara, D. M.; Montblanch, A. R.-P.; Barbone, M.; Latawiec, P.; Yoon, D.; Ott, A. K.; Loncar, M.; Ferrari, A. C.; Atature, M. Large-scale quantum-emitter arrays in atomically thin semiconductors. *Nat. Commun.* **2017**, *8* (1), 15093.
(22) Parto, K.; Azzam, S. I.; Banerjee, K.; Moody, G. Defect and strain engineering of monolayer WSe_2 enables site-controlled single-photon emission up to 150 K. *Nat. Commun.* **2021**, *12* (1), 3585.
(23) Luo, Y.; Liu, N.; Li, X.; Hone, J. C; Strauf, S. Single photon emission in WSe_2 up 160 K by quantum yield control. *2D Materials* **2019**, *6* (3), 035017.
(24) So, J.-P.; Jeong, K.-Y.; Lee, J. M.; Kim, K.-H.; Lee, S.-J.; Huh, W.; Kim, H.-R.; Choi, J.-H.; Kim, J. M.; Kim, Y. S.; Lee, C.-H.; Nam, S.; Park, H.-G. Polarization Control of Deterministic Single-Photon Emitters in Monolayer WSe_2. *Nano Lett.* **2021**, *21* (3), 1546.
(25) Kumar, S.; Kaczmarczyk, A.; Gerardot, B. D. Strain-Induced Spatial and Spectral Isolation of Quantum Emitters in Mono- and Bilayer WSe_2. *Nano Lett.* **2015**, *15* (11), 7567.
(26) Flatten, L. C.; Weng, L.; Branny, A.; Johnson, S.; Dolan, P. R.; Trichet, A. A. P.; Gerardot, B. D.; Smith, J. M. Microcavity enhanced single photon emission from two-dimensional WSe_2. *Appl. Phys. Lett.* **2018**, *112* (19), 191105.
(27) Hoang, T. B.; Akselrod, G. M.; Mikkelsen, M. H. Ultrafast Room-Temperature Single Photon Emission from Quantum Dots Coupled to Plasmonic Nanocavities. *Nano Lett.* **2016**, *16* (1), 270.
(28) Sapienza, L.; Davanco, M.; Badolato, A.; Srinivasan, K. Nanoscale optical positioning of single quantum dots for bright and pure single-photon emission. *Nat. Commun.* **2015**, *6* (1), 7833.
(29) Aharonovich, I.; Englund, D.; Toth, M. Solid-state single-photon emitters. *Nat. Photonics* **2016**, *10* (10), 631.
(30) Gupta, S.; Wu, W.; Huang, S.; Yakobson, B. I. Single-Photon Emission from Two-Dimensional Materials, to a Brighter Future. *J. Phys. Chem. Lett.* **2023**, *14* (13), 3274.
(31) Proscia, N. V.; Shotan, Z.; Jayakumar, H.; Reddy, P.; Cohen, C.; Dollar, M.; Alkauskas, A.; Doherty, M.; Meriles, C. A.; Menon, V. M. Near-deterministic activation of room-temperature quantum emitters in hexagonal boron nitride. *Optica* **2018**, *5* (9), 1128.
(32) Lee, Y.; Tran, T. T.; Kim, Y.; Roy, S.; Taniguchi, T.; Watanabe, K.; Jang, J. I.; Kim, J. Enhanced Radiative Exciton Recombination in Monolayer WS_2 on the hBN Substrate Competing with Nonradiative Exciton-Exciton Annihilation. *ACS Photonics* **2022**, *9* (3), 873.
(33) Hoshi, Y.; Kuroda, T.; Okada, M.; Moriya, R.; Masubuchi, S.; Watanabe, K.; Taniguchi, T.; Kitaura, R.; Machida, T. Suppression of exciton-exciton annihilation in tungsten disulfide monolayers encapsulated by hexagonal boron nitrides. *Phys. Rev. B* **2017**, *95* (24), 241403.
(34) Chatterjee, S.; Gupta, G.; Das, S.; Watanabe, K.; Taniguchi, T.; Majumdar, K. Trion-trion annihilation in monolayer WS_2. *Phys. Rev. B* **2022**, *105* (12), L121409.
(35) Chaudhary, R.; Raghunathan, V.; Majumdar, K. Origin of selective enhancement of sharp defect emission lines in monolayer WSe_2 on rough metal substrate. *J. Appl. Phys.* **2020**, *127* (7), 073105.
(36) Simon, C.; Afzelius, M.; Appel, J.; Boyer De La Giroday, A.; Dewhurst, S. J.; Gisin, N.; Hu, C. Y.; Jelezko, F.; Kröll, S.; Müller, J. H.; Nunn, J.; Polzik, E. S.; Rarity, J. G.; De Riedmatten, H.; Rosenfeld, W.; Shields, A. J.; Sköld, N.; Stevenson, R. M.; Thew, R.; Walmsley, I. A.; Weber, M. C.; Weinfurter, H.; Wrachtrup, J.; Young, R. J. Quantum memories: A review based on the European integrated project "Qubit Applications (QAP). *European Physical Journal D* **2010**, *58* (1), 1.
(37) Gao, T.; von Helversen, M.; Anton-Solanas, C.; Schneider, C.; Heindel, T. Atomically-thin single-photon sources for quantum communication. *npj 2D Materials and Applications* **2023**, *7* (1), 4.
(38) Peng, L.; Chan, H.; Choo, P.; Odom, T. W.; Sankaranarayanan, S. K. R. S.; Ma, X. Creation of Single-Photon Emitters in WSe_2 Monolayers Using Nanometer-Sized Gold Tips. *Nano Lett.* **2020**, *20* (8), 5866.
(39) Wang, Q.; Maisch, J.; Tang, F.; Zhao, D.; Yang, S.; Joos, R.; Portalupi, S. L.; Michler, P.; Smet, J. H. Highly Polarized Single Photons from Strain-Induced Quasi-1D Localized Excitons in WSe_2. *Nano Lett.* **2021**, *21* (17), 7175.

https://doi.org/10.1021/acs.nanolett.4c03168
Nano Lett. 2024, 24, 12461−12468

(40) Shepard, G. D; Ajayi, O. A; Li, X.; Zhu, X-Y; Hone, J.; Strauf, S. Nanobubble induced formation of quantum emitters in monolayer semiconductors. *2D Materials* **2017**, *4* (2), 021019.
(41) Srivastava, A.; Sidler, M.; Allain, A. V.; Lembke, D. S.; Kis, A.; Imamoglu, A. Optically active quantum dots in monolayer WSe_2. *Nat. Nanotechnol.* **2015**, *10* (6), 491.
(42) Rosenberger, M. R.; Dass, C. K.; Chuang, H.-J.; Sivaram, S. V.; McCreary, K. M.; Hendrickson, J. R.; Jonker, B. T. Quantum Calligraphy: Writing Single-Photon Emitters in a Two-Dimensional Materials Platform. *ACS Nano* **2019**, *13* (1), 904.
(43) Hernandez Lopez, P.; Heeg, S.; Schattauer, C.; Kovalchuk, S.; Kumar, A.; Bock, D. J.; Kirchhof, J. N.; Hofer, B.; Greben, K.; Yagodkin, D.; Linhart, L.; Libisch, F.; Bolotin, K. I. Strain control of hybridization between dark and localized excitons in a 2D semiconductor. *Nat. Commun.* **2022**, *13* (1), 7691.
(44) Abramov, A. N.; Chestnov, I. Y.; Alimova, E. S.; Ivanova, T.; Mukhin, I. S.; Krizhanovskii, D. N.; Shelykh, I. A.; Iorsh, I. V.; Kravtsov, V. Photoluminescence imaging of single photon emitters within nanoscale strain profiles in monolayer WSe_2. *Nat. Commun.* **2023**, *14* (1), 5737.
(45) Moon, H.; Bersin, E.; Chakraborty, C.; Lu, A.-Y.; Grosso, G.; Kong, J.; Englund, D. Strain-Correlated Localized Exciton Energy in Atomically Thin Semiconductors. *ACS Photonics* **2020**, *7* (5), 1135.
(46) Xu, D. D.; Vong, A. F.; Lebedev, D.; Ananth, R.; Wong, A. M.; Brown, P. T.; Hersam, M. C.; Mirkin, C. A.; Weiss, E. A. Conversion of Classical Light Emission from a Nanoparticle-Strained WSe_2 Monolayer into Quantum Light Emission via Electron Beam Irradiation. *Adv. Mater.* **2023**, *35* (5), 2208066.
(47) Linhart, L.; Paur, M.; Smejkal, V.; Burgdorfer, J.; Mueller, T.; Libisch, F. Localized Intervalley Defect Excitons as Single-Photon Emitters in WSe_2. *Phys. Rev. Lett.* **2019**, *123* (14), 146401.

https://doi.org/10.1021/acs.nanolett.4c03168
Nano Lett. 2024, 24, 12461−12468